J Mater Sci (2012) 47:151–161
DOI 10.1007/s10853-011-5782-3

Formability of thermally cured and of nanoclay-reinforced polyelectrolyte films on NiTi substrates

J. Lackmann · T. Niendorf · M. Maxisch ·
R. Regenspurger · G. Grundmeier ·
H. J. Maier

Received: 7 June 2011 / Accepted: 11 July 2011 / Published online: 29 July 2011

Abstract The present study characterizes the formability of thin polyelectrolyte films which were modified by curing and alternatively reinforced with nano-sized clay-platelets. To investigate the suitability of modified polyelectrolyte coatings for biomedical applications, films were applied on both the polycrystalline and single crystal NiTi 50.9 at.% substrates and mechanically deformed in simulated body fluid (Hank's solution) under cyclic tensile loading. In situ electron backscatter diffraction, in situ confocal laser scanning microscopy, photoelastic-modulated infrared reflection absorption spectroscopy, and ellipsometry measurements were employed to study defect formation. Based on observations from the substrates and films, conducted before and after to mechanical testing, defect formation during tensile cycling was related to substrate and film characteristics. Defects emerged particularly in unmodified and cured polyelectrolyte films on both polycrystalline and single crystalline substrates within areas of pronounced topographic changes. In contrast, the nanoclay-modified coatings remained defect free, indicating a remarkable improvement of formability, which can be related to the reinforcing clay-platelets within the polyelectrolyte matrix.

Introduction

Based on the stress- or thermally induced reversible austenitic (B2) to martensitic (B19′) phase transformations, nickel–titanium shape memory alloys (SMAs) provide high recoverable superelastic strains. In addition, NiTi SMAs are known to be biocompatible [1, 2], rendering these materials appropriate for various biomedical applications. Thus, NiTi SMAs are utilized for the fabrication of clinical instruments and components such as self expanding stents, dental implants, bone anchors, or tendons [2–5]. As nickel is a potential toxin within the human body [6], which may cause degeneration of muscle tissue and allergic responses [7], the use of NiTi for long-term implants is still controversial. Although numerous studies have shown that Ni-release typically remains marginal during implantation because of the formation of an adherent passive oxide [8–12], increased Ni-release cannot be excluded because of the high pitting corrosion sensitivity of untreated implant surfaces [13]. Even well-adjusted, low nickel-content surfaces obtained by surface treatments such as electro-polishing, chemical passivation [11] or selective oxidation [14] are potential sources for Ni-release from buried, nickel-rich sublayers [15]. Thus, additional coatings are required to provide a sufficient protection from long-term Ni-release.

Recently, different ceramic coating systems, such as TiN, ZrO_2, Al_20_3, and diamond-like carbon (DLC), have been successfully applied on NiTi substrates; however, although a remarkable increase of the breakdown potential was observed, these studies did neither consider the particular mechanical requirements of coatings for biomedical implants [16–18] nor revealed a sufficient formability of the brittle coating materials [19].

Clearly, a coating is needed, which matches the requirements of slender implant structures as well as the

---

J. Lackmann (✉) · T. Niendorf · H. J. Maier
Lehrstuhl für Werkstoffkunde (Materials Science), University of Paderborn, Pohlweg 47-49, 33098 Paderborn, Germany
e-mail: jan.lackmann@mail.upb.de

M. Maxisch · R. Regenspurger · G. Grundmeier
Technical and Macromolecular Chemistry, Department of Chemistry, University of Paderborn, Warburger Straße 100, D-33098 Paderborn, Germany

large superelastic strains caused by implant deployment and strains induced by the pulsating nature of the blood stream [20]. Recently, it has been demonstrated that layer-by-layer (LBL) polyelectrolyte coatings are capable of matching some of these requirements [21]. The formation of polyelectrolyte coatings such as polyacrylic acid (PAA)/polyallylamine hydrochloride (PAH), was introduced by Decher et al. [22]. Owing to the electrostatic adsorption of anionic and cationic polyelectrolytes, polyelectrolyte films can be applied on complex structures by means of alternating dip coating from charged solutions [23, 24]. Furthermore, polyelectrolyte films can combine good elastic, biocompatible [25], as well as barrier properties [26], rendering them particularly interesting as a coating material for biomedical implants. For more detailed information regarding the properties of polyelectrolyte coatings, the reader is referred to [27, 28].

Although a related study revealed that polyelectrolyte coatings applied on polycrystalline NiTi remained defect free under monotonic strains up to 5%, cyclic loading in the pseudoelastic regime resulted in the formation of several small defects within the vicinity of grain boundaries after 300 cycles [21]. It was demonstrated that film failure can be attributed to topographic evolution along the boundaries between highly misoriented grains, which emerge because of phase transformation-induced strain inhomogeneities [29]. For long-term implants, defect formation cannot be tolerated as even small uncoated sample sections may act as a starting point for corrosion and related Ni-release [19]. In order to improve the coating system, both the properties of the polyelectrolyte films as well as the substrate material need to be considered.

Hence, the polyelectrolyte films investigated in the present study were modified by heat treatment as well as by reinforcement of the polyelectrolyte matrix with nano-sized clay-platelets. Several studies have addressed the improvement of film characteristics, such as stiffness and barrier properties by heat treatments and the related change from electrostatic to covalent bonding (e.g., [26, 30]). Similar improvements have been demonstrated for reinforcement of polyelectrolyte films with clay-platelets e.g., [31, 32]. Although an improvement of the film integrity during cyclic superelastic deformation of the substrate can be expected based on these studies, to the best of the authors' knowledge this aspect has not been investigated so far.

As the change in topography across grain boundaries has been shown to determine the defect formation in thin polyelectrolyte films [21], more attention should also be put on the evolution of topography during forward and reverse transformations of the NiTi-substrate. Given this scenario, single crystals were also used as grain boundary-free reference substrate. The present study provides an analysis of the chemistry of the investigated film modifications as well as an investigation of the substrate's surface evolution employing in situ tests. The data obtained demonstrate a substantial effect of the nanoclay on formability of the polyelectrolyte films.

Experimental details

Substrate preparation and characterization

Dog bone-shaped samples with a total length of 28 mm and a gauge section of $9.6 \times 2.8 \times 2.6$ mm^3 were electro-discharge machined (EDM) from a 50.9 at.% NiTi single crystal bar grown by the Bridgman technique in He environment. The tensile axis of the samples was along the [111] orientation, which implied minimum critical stresses for phase transformation in tension [33]. Polycrystalline dog bone-shaped samples with a total length of 32 mm and a gauge section of $6 \times 1.6 \times 1.5$ mm^3 were machined from a polycrystalline bar of the same chemical composition. Electron back scatter diffraction (EBSD) measurements revealed that a moderate [111] texture was present along the tensile axis. For pre-characterization of the polyelectrolyte films by photoelastic-modulated infrared reflection absorption spectroscopy (PM-IRRAS) and ellipsometry, quadratic samples with $20 \times 20 \times 2$ mm^3 were cut from the polycrystalline bulk NiTi.

In order to obtain a stable and fully recoverable stress–strain response, the dog bone-shaped samples were solutionized and subsequently aged at 823 K for 1.5 h (single crystals) and at 650 K for 1.5 h (polycrystals). These heat treatments resulted in large ($\approx$500 nm), incoherent Ti_3Ni_4 precipitates at 823 K and small ($\approx$10 nm), coherent precipitates at an aging temperature of 650 K [34]. Although the larger precipitates resulted in a less stable stress–strain response as compared with the small precipitates, the additional decrease of the critical transformation stress was mandatory for the single crystals as elevated critical stress levels resulted in premature brittle fracture. Consequently, the test temperature during pseudoelastic straining was held at 293 K, although 310 K would be preferable regarding biomedical applications. However, given the Clausius–Clapeyron slope of 7.9 MPa K^{-1} [35], this temperature change would have raised the critical transformation stress to 360 MPa, which is not compatible with the mechanical response of the single crystals employed. Figure 1 depicts the resulting stress–strain response of a single crystal (full line) and polycrystalline (dashed line) NiTi sample when strained up to 5%. Both microstructures demonstrated fully recoverable pseudoelastic strains at room temperature, while the initial critical stress levels were found to be 225 MPa for single crystals and 245 MPa for polycrystals. It is important to mention that the critical

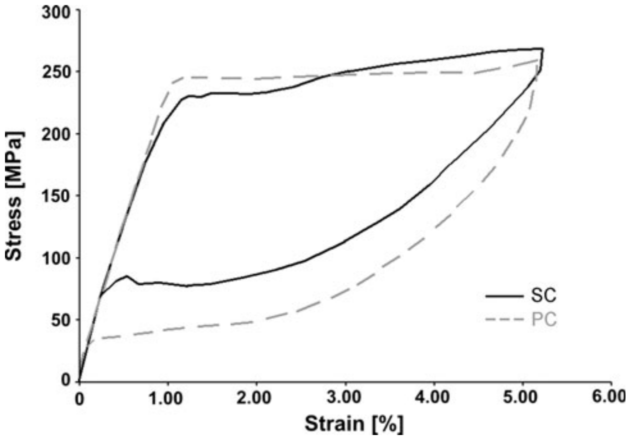

Fig. 1 Stress–strain response of polycrystalline (*dashed line*) and single crystal (*full line*) 50.9 at.% NiTi at 293 K

stress levels decreased slightly during cycling for both the single crystal and polycrystalline samples; however, fully recoverable strains of 5% were still achieved even after several hundred cycles. The larger stress hysteresis of the polycrystalline NiTi can be attributed to elastic energy dissipation at the grain boundaries during phase transformation. Sample surfaces were subjected to mechanical and electro-polishing using an electrolyte containing 6% perchloric acid, 34% buthanol and 60% methanol. To remove any residue from the surfaces, samples were exposed to tetrahydrofuran, isopropanol, and ethanol (analytical grade) for 10 min in an ultrasonic bath and subsequently rinsed with pure ethanol and dried under a nitrogen stream.

Polyelectrolyte film preparation and characterization

Polyacrylic acid (PAA)/polyallylamine hydrochloride (PAH) was chosen as the basic coating system since the properties and the parameters for processing films from these materials are well understood. Polyallylamine hydrochloride (PAH, molecular weight (Mw) 70,000, Aldrich) and polyacrylic acid (PAA, Mw 100,000, Aldrich) were used without any further purification. Ultrapure water (resistivity 18 MΩ cm) was used to prepare polyelectrolyte solutions for the multilayer assembly with a concentration of 0.01 M on a repeat unit basis. For preparation of all the polyelectrolyte films investigated in the present study, the polyelectrolyte solutions were adjusted to pH7.

Coatings were assembled using a dip coater (Nima Technology, UK) by immersing the bare substrate alternately in polyanion and polycation solutions for 5 min. In between, the samples were rinsed with water for 5 min in order to remove any loose material from the surface. By repeating this procedure, ten bilayers of PAA/PAH were assembled which will be referred to as $[PAA/PAH]_{10}$-pH7 in the unmodified state. According to heat treatments suggested in the literature [36], samples coated with unmodified films were cured at 230 °C in N_2 environment for 2 h, hereafter referred to as $[PAA/PAH]_{10}$-pH7-cured. For the preparation of nanoclay-reinforced films, montmorillionite (MMT) was purchased from Südchemie and exfoliated in water by stirring for several days. After sedimentation for 2 days the supernatant was utilized to form a 10:1 aqueous solution. Nanoclay polyelectroyte films were made by alternated dipping in MMT, PAA, and PAH solutions to form trilayers of MMT/PAA/PAH. The montmorillionite-reinforced films will be referred to as $[MMT/PAA/PAH]_{10}$-pH7 in the present study. In addition, a combination of MMT-reinforcement and curing was employed. The glass transition temperatures (T_g) of the polyelectrolytes used are 80 °C for PAA and 190 °C for PAH [37]. Since increased densities of cross-linking due to thermally induced covalent bonding result in elevated transition temperatures, the formability of all film modifications was investigated below T_g.

In order to characterize the surface chemistry of the coated substrates and to investigate the initial film thickness of the modified polyelectrolyte films, PM-IRRAS and ellipsometry measurements were carried out. All the PM-IRRAS measurements were conducted using a Vertex70/PMA50 (Bruker Optik GmbH, Germany). The spectra were recorded with a resolution of 4 cm^{-1} and averaged over 512 scans. The angle of incidence was set to 80°, and for the photoelastic modulator, a maximum efficiency of 3,000 with 1,500 cm^{-1} was chosen. The spectra were processed using OPUS software (Bruker Optik GmbH, Germany) and manually baseline corrected.

Ellipsometry experiments were performed with an EP^3-ellipsometer (Nanofilm, Germany) equipped with a laser with a wavelength of 532 nm. The angle of incidence was set to 42° and four measurements were done and averaged for each sample.

Mechanical and microscopic characterizations of bare and coated substrates

In situ characterization of the surface alterations and microstructural features of the bare substrates was carried out using a miniature load frame capable of ±10 kN in combination with a violet laser ($\lambda = 408$ nm) confocal laser scanning microscope (CLSM) and an EBSD system operated within a scanning electron microscope (SEM). EBSD measurements within areas of 90×90 mm^2 were conducted for both the microstructures at $\varepsilon = 3\%$ and $\varepsilon = 1.5\%$ during forward and reverse transformations. The SEM was operated with an acceleration voltage of 20 kV and a step size of 0.5 µm for the EBSD measurements. Furthermore, CLSM measurements were carried out on the uncoated substrates subsequent to the EBSD scans. Intensity batches were recorded during forward and reverse transformations at strain intervals of approximately 0.5%, using a 1,000 × objective lens with a numerical aperture of 0.95 and a working distance of 0.2 mm, featuring an axial resolution of 10 nm. Topographical alterations during forward and reverse transformation were directly calculated from the obtained batches.

Cyclic mechanical experiments were carried out using the miniature load frame in combination with a custom-built-setup for testing in liquid media. A PMMA-container was mounted under the sample grips and silicone was employed to realize a leak-free but ductile seal between the container and the grips. Detailed information including a schematic of the experimental set-up can be found in a related study [21]. The PMMA container was filled with Hank's solution such that the sample surface was covered with about 1 mm solution. The composition of the solution used in the present study was adopted from the study of Choubey et al. [38]. As water uptake and softening effects in the presence of salt ions are known to have an impact on the mechanical properties of polyelectrolyte assemblies (e.g., [39, 40]), all the samples were subjected to the solution 0.5 h before strains were applied, since an equilibrium state should be reached after this immersion time according to Tanchak and Barrett [41]. Mechanical cyclic experiments employing a preliminary immersion time of 24 h revealed no differences regarding the formability of the polyelectrolyte films as compared to the results presented in this article. After the initial immersion, tensile cycling up to $\varepsilon = 5\%$ (Fig. 1) was carried out for substrates coated with $[\mathrm{PAA/PAH}]_{10}$-pH7, $[\mathrm{PAA/PAH}]_{10}$-pH7-cured, $[\mathrm{MMT/PAA/PAH}]_{10}$-pH7, and $[\mathrm{MMT/PAA/PAH}]_{10}$-pH7-cured films. For the polycrystalline substrates, 300 cycles at a strain rate of $\dot{\varepsilon} = 2 \cdot 10^{-3} s^{-1}$ were conducted, while only 50 cycles were carried out for the single crystal substrates. The reason for the different number of cycles will be explained based on the observed surface alteration characteristics of the different substrates presented in "Pre-characterization of bare substrates" Section. After the mechanical cycling, CLSM images were recorded from the sample surfaces directly after removing the solution from the container.

The CLSM data demonstrated that within the gauge section, all areas behaved similarly. In contrast, topographic evolutions in the interior of the grains and at the grain boundaries are different [29]. Therefore, defect formation on the polycrystalline substrates was documented within the areas of maximum topographic changes along critical grain boundaries to ensure the comparability of the observations on the different film modifications. Post-deformation microstructural investigations were feasible as good quality EBSD patterns were obtained even from the coated substrates. At least two samples of each substrate–film system were tested to check for sample-to-sample variations. CLSM imaging on apparently unaffected films was supplemented by atomic force microscopy (AFM), which provided for an increased vertical resolution in the sub-nanometer scale. AFM topography imaging was performed using a JPK Nanowizard II Ultra System (JPK Instruments, Germany). The system was equipped with an antinoise and antivibration box to minimize environmental influences during imaging. All the AFM-measurements were performed in intermittent contact mode under ambient conditions in air using NSC15-type cantilevers (Mikromash, Estonia) with a resonance frequency of about 320 kHz and a force constant of 40 N/m. AFM imaging was conducted at a constant amplitude, which was damped to 98–90% of the free amplitude for optimal sample–tip interaction. The scan speed was adjusted between 1 and 2 μm per second, at a scan resolution of 512 × 512 pixels.

Results

Characterization of the initial chemistry and thickness of polyelectrolyte films

Schematic assemblies and corresponding PM-IRRAS measurements of the film modifications investigated in the present study are depicted in Fig. 2. Figure 2a shows the schematic assembly of unmodified $[\mathrm{PAA/PAH}]_{10}$-pH7. The peaks at 1,580 and 1,407 cm^{-1} can be assigned to the asymmetric and symmetric stretch vibrations, respectively, of the deprotonated carboxyl group [26]. The peaks at 2,939 and 2,864 cm^{-1} belong to the asymmetric and symmetric stretch vibrations of CH_2 of the chain, respectively. The broad peak centered at 3,434 cm^{-1} is assigned to NH and OH vibration modes. The signal at 1,634 cm^{-1} is assigned to the NH deformation vibration [42]. The individual layers of PAA and PAH adhere to each other through electrostatic in addition to van-der-Waals forces. The thickness of the polyelectrolyte layer was determined as 80 ± 10 nm by ellipsometry.

After the tempering process (Fig. 2b), the chemical structure of the polyelectrolyte layer changed significantly. The signals for OH and CH_2 vibrations remained, whereas the peak intensities for COO^- and NH vibrations are replaced by signals at 1,666 and 1,550 cm^{-1}, respectively, corresponding to an amide bond [36]. The peak at 1,726 cm^{-1} indicates remaining COOH groups [26]. Thickness measurements revealed a small decrease in layer thickness to 65 ± 10 nm.

In the case of $[\mathrm{MMT/PAA/PAH}]_{10}$-pH7, the spectra included additional signals for Si–O–Si (1,097 cm^{-1}) and

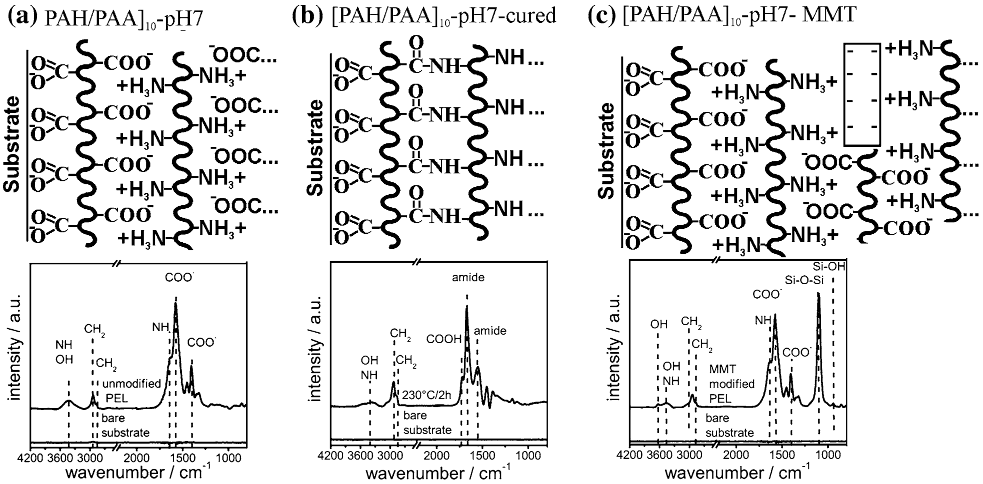

Fig. 2 Schematic film assembly and corresponding PM-IRRAS spectra of **a** unmodified PAA/PAH films, **b** cured PAA/PAH films, and **c** MMT-reinforced PAA/PAH films

Si–OH (940 cm^{-1}) bonds [43] corresponding to incorporated MMT particles [44]. The layer thickness was determined to be 75 ± 10 nm.

Pre-characterization of bare substrates

In order to characterize the phase transformation-induced surface evolution during pseudoelastic cycling, in situ EBSD and CLSM measurements were carried out. A previous study had revealed that topography evolution at grain boundaries is the main mechanism for defect formation in [PAA/PAH]-coated polycrystalline NiTi substrates [21] and detailed in situ experiments demonstrated that topography-induced strains can be higher by one order of magnitude compared with global strains when measured by digital image correlation [29]. In order to shed light on phase boundary effects, microstructural and topographic evolutions during the whole forward and reverse transformations were determined on polycrystalline and single crystal substrates.

Figure 3 depicts EBSD image quality patterns of a polycrystalline NiTi microstructure during forward (Fig. 3a) and reverse (Fig. 3b) transformations. EBSD measurements were carried out during maximum transformation activity within the near-[111]-oriented grain shown in the center of Fig. 3a, b. Comparing Fig. 3a with 3b,

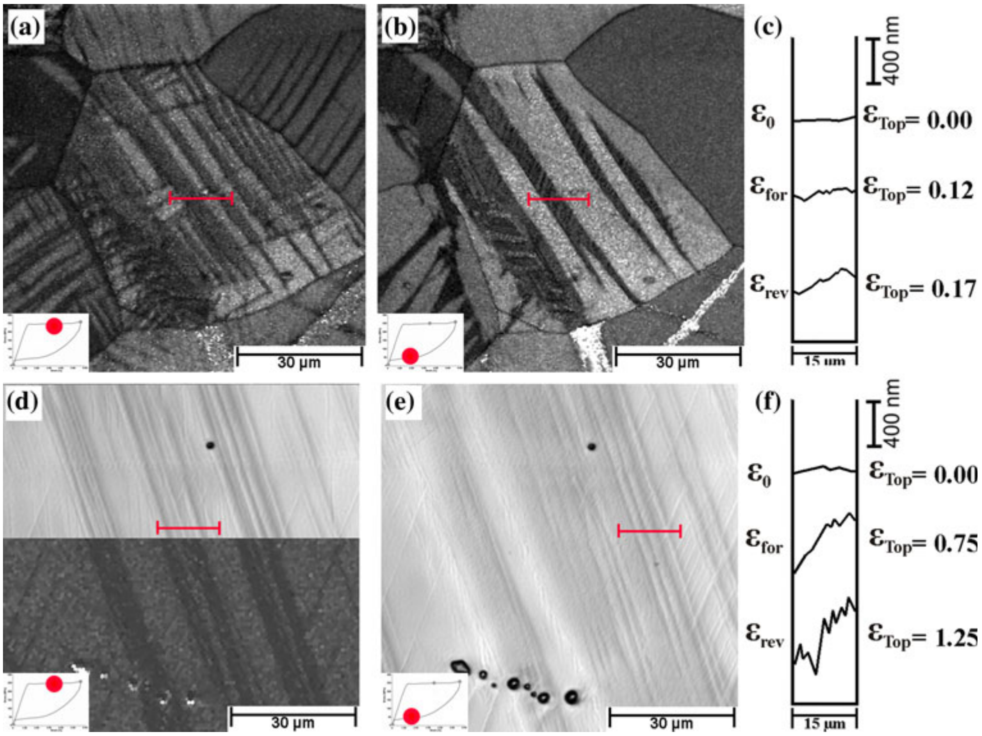

Fig. 3 In situ EBSD quality images recorded from a polycrystalline NiTi substrate during **a** forward and **b** reverse transformations. In situ observations for single crystal NiTi during **d** forward and **e** reverse transformation supplemented by CLSM measurements. The reliefs shown in figure **c** and **f** correspond to the topographic measurements along the phase boundaries present during forward and reverse transformations indicated by the *red lines*. Stress axis is *horizontal* (Color figure online)

fundamental differences in the morphology of surface martensite during forward and reverse transformation are revealed. Numerous martensite plates appear in a slender, lenticular form during loading. Two different variants were determined from the EBSD data. The predominant variant forms plates along a 60° angle relative to the loading axis. Based on the crystallography measured using EBSD and in situ TEM observations on polycrystalline NiTi samples reported by Tirry and Schryvers [45] the formation of [1 -1 0]-B19′ martensite from [111]-oriented B2-austenite dominates. Although strain incompatibilities at the grain boundaries are reduced within the investigated area (Fig. 3a, b) because of minor transformation strain differences, some minor grain boundary effects can be observed, cf. the grain in the lower left of Fig. 3a, b. During unloading (Fig. 3b), solely the [1 -1 0]-B19′ system was detectable within the austenite matrix. Compared with the martensite morphology during loading, fewer but wider plates were present (Fig. 3b).

In the following, topography effects associated with phase boundary motion are investigated regarding their impact on the formation of defects in the thin films. High resolution CLSM data recorded along the red lines in Fig. 3a (ε_{for}) and 3b (ε_{rev}) are plotted in Fig. 3c, where ε_0 marks the initial relief in the undeformed state. Following the approach employed to quantify the topography effect at grain boundaries in polycrystalline NiTi [29], the lengths of the profiles measured across the phase boundaries during forward and reverse transformations were related to the initial profile lengths. Profile length elongations of 12 and 17% during loading and unloading, respectively, indicate that phase boundary topographies are more relevant for defect formation in the applied films than lateral local strains, which range between 6–10% [29]. Interestingly, the topography is more pronounced during reverse transformation, which will be discussed regarding geometric and interfacial properties of the martensite in Chapter 4.

The lower part of Fig. 3d shows an image quality scan obtained on a single crystal with the martensite fronts passing through. The scan reveals the presence of a dominant variant and a secondary variant. The EBSD data indicated that the same main variant as in the polycrystalline near-[111] austenite grain is forming, although a small deviation regarding the angle between load axis and martensite front could be observed. Phase transformation was easily detectable by CLSM because of the larger topography effects (Fig. 3f) observed during forward (Fig. 3d) and reverse transformations (Fig. 3e). During unloading (Fig. 3e), the intensity image reveals the presence of a wider martensitic front, indicated by the darker surface area. The measured maximum height differences of 500 and 800 nm can be converted to local profile-related elongations of 75 and 125% during loading and unloading, respectively. Although these calculations are strongly dependent on the length of the considered profile, the results shown in Fig. 3f, which were calculated based on an initial profile length of 15 µm for both substrates, indicate that topography-induced strains are one order of magnitude higher in the single crystals as compared with the polycrystalline substrates. Based on the data obtained, it is assumed that a phase boundary-related topography change is the governing mechanism for defect formation in thin films applied onto single crystal NiTi substrates.

Figure 4 summarizes the evolution of maximum surface topography with macroscopic strains during forward and reverse transformations measured across phase boundaries on the polycrystalline sample shown in Fig. 3a, b (diamonds) and interfaces on the single crystal sample shown in Fig. 3d, e (squares). In addition, the topographic evolution across a boundary between highly misoriented grains recorded from a polycrystalline substrate is also included (dots). All graphs show elevated reliefs emerging mainly between 2 and 5% strains, although the stress–strain response in Fig. 1 indicates the onset of the martensite formation at approximately 1% macroscopic strain. This can be related to the fact that martensite nucleation is often triggered by stress peaks present near the sample grips (e.g., [46]) and, thus, first transformation within the center of the gauge section is only observed at larger macroscopic strains. For both substrates, the largest topographic changes at phase

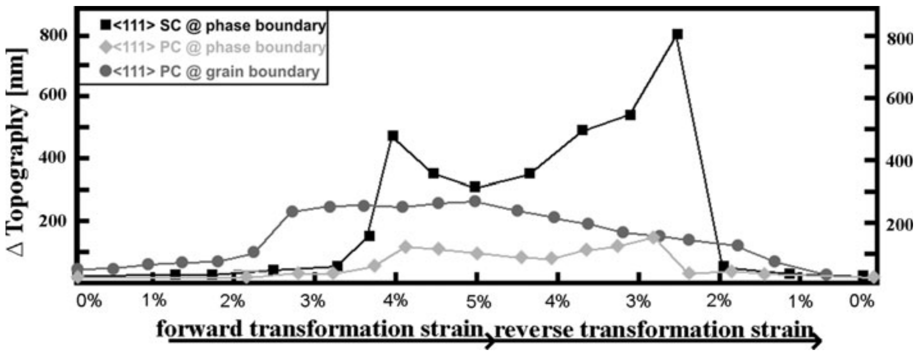

Fig. 4 Maximum topography heights measured along phase boundaries on polycrystalline (*diamonds*) and single crystal substrates (*squares*) as well as across a highly misoriented grain boundary (*dots*) during forward and reverse transformation

boundaries are present during initial forward and final reverse transformations. For both the single crystal and the polycrystalline substrates, effects are higher during reverse transformation while the topographic reliefs were always more prominent in the single crystals. Comparing the surface evolution on the polycrystalline substrates, it becomes apparent that topography effects are higher along grain boundaries than at phase boundaries, which is in good agreement with recent results on the formation of defects in thin polyelectrolyte coatings on polycrystalline substrates [21].

Altogether, the results presented in this section characterize and quantify the prevailing conditions on polycrystalline and single crystal substrates during forward and reverse transformations. Therefore, the formability and the defect formation within different polyelectrolyte film modifications can be compared, even though the different coating modifications could not be tested on exactly the same sample surface.

Characterization of polyelectrolyte film–substrate systems

Figure 5 summarizes the microscopic observations subsequent to straining in Hank's solution. The polycrystalline substrates coated with polyelectrolyte in the unmodified and modified states are depicted in the left part of Fig. 5. The untreated $[PAA/PAH]_{10}$-pH7 films demonstrated good formability and only few "spot-like" defects were observed (bright spots) after 300 cycles. Defects formed predominantly in the vicinity of those grain boundaries that were determined to be critical according to the topographic evolution shown in Fig. 4. Curing of the polyelectrolyte coatings lowered the formability performance remarkably. As shown in fig. 5b, large "crack-like" defects formed predominantly perpendicular to the loading axis to such an extent that delamination of the polyelectrolyte film was observed. Apparently, pronounced crack formation and delamination took place at an early deformation state, and most defects showed no clear relation to the microstructural features. It is supposed that the extensive cracking and delamination resulted in permanent relaxation of the thermally cured films, and therefore no further defect formation along otherwise critical topographies occurred. In contrast, a positive impact of the nanoclay reinforcement on the formability of $[MMT/PAA/PAH]_{10}$-pH7 polyelectrolyte is demonstrated in Fig. 5c. Although an elevated topographic formation was observed along the grain boundary marked in red, 300 strain cycles did not induce any microscopically traceable defects. Interestingly, the composite of cured $[PAA/PAH]_{10}$-pH7 including nanoclays (Fig. 5d) shows "crack-like" defect formation, indicating that in particular the covalent bonds reduce the formability.

The polyelectrolyte films that were applied on the single crystals were subjected to only 50 cycles, as accelerated defect formation was observed because of elevated topographic effects at phase boundaries (Fig. 4). The topographic evolution resulted in the formation of slender, "crack-like" defects along the phase boundaries in unmodified $[PAA/PAH]_{10}$-pH7 films as seen in Fig. 5e. This demonstrates the detrimental impact of the large height differences on the single crystal substrates as compared with the polycrystalline specimens (Fig. 5a). Furthermore, $[PAA/PAH]_{10}$-pH7-cured films revealed distinct cracks emerging in a "grid-like" pattern (Fig. 5f) oriented along the same direction as the phase fronts shown in Fig. 3d, e. These defects can certainly be related to phase front induced effects; however, in contrast to the polycrystalline substrate (Fig. 5b), no delamination was observed. Hence, it can be assumed that the elevated accumulated strains in the polycrystals due to the higher cycle number finally caused flaking of the polyelectrolyte films.

Confirming the results from the polycrystalline substrates (Fig. 5c), $[MMT/PAA/PAH]_{10}$-pH7 films showed no defects after straining on the single crystal substrates (Fig. 5g), demonstrating that nanoclay-reinforced films can even endure extreme changes in surface topography. It is noteworthy to mention that the tiny spots seen in Fig. 5g are artifacts from the LBL-assembly and were already present before straining. Interestingly, the combination of MMT-reinforcement and curing shown in Fig. 5h resulted in a remarkably reduced defect formation on the single crystals as compared to the purely cured films (Fig. 5f) and films of the same type on polycrystals (Fig. 5d). This can be related to the positive impact of the nanoclay as well as the lower number of cycles and, hence, a smaller accumulated strain in case of the single crystal substrates.

A distinct impact of phase boundary effects was observed for single crystal substrates while defect formation on polycrystals was predominantly triggered by accumulated local strains at grain boundaries. Unmodified $[PAA/PAH]_{10}$-pH7 films demonstrated good formability revealing a few defects along grain or phase boundaries. In contrast, covalent bonding induced by heat treatment had a negative impact on the formability on both substrates. However, nanoclays included into an electrostatically bonded polyelectrolyte matrix resulted in a remarkable improvement of formability as observed for both substrates. As no defects were observable in the microscope images (Fig. 5c, g), additional AFM-images were recorded from $[MMT/PAA/PAH]_{10}$-pH7-coated polycrystalline NiTi prior (Fig. 6a) and subsequent (Fig. 6b) to straining to provide higher resolution data. In the initial state, the coated surface formed a "dome-like" structure revealing a root-mean-squared roughness (RMS) of 3.8 nm, which is

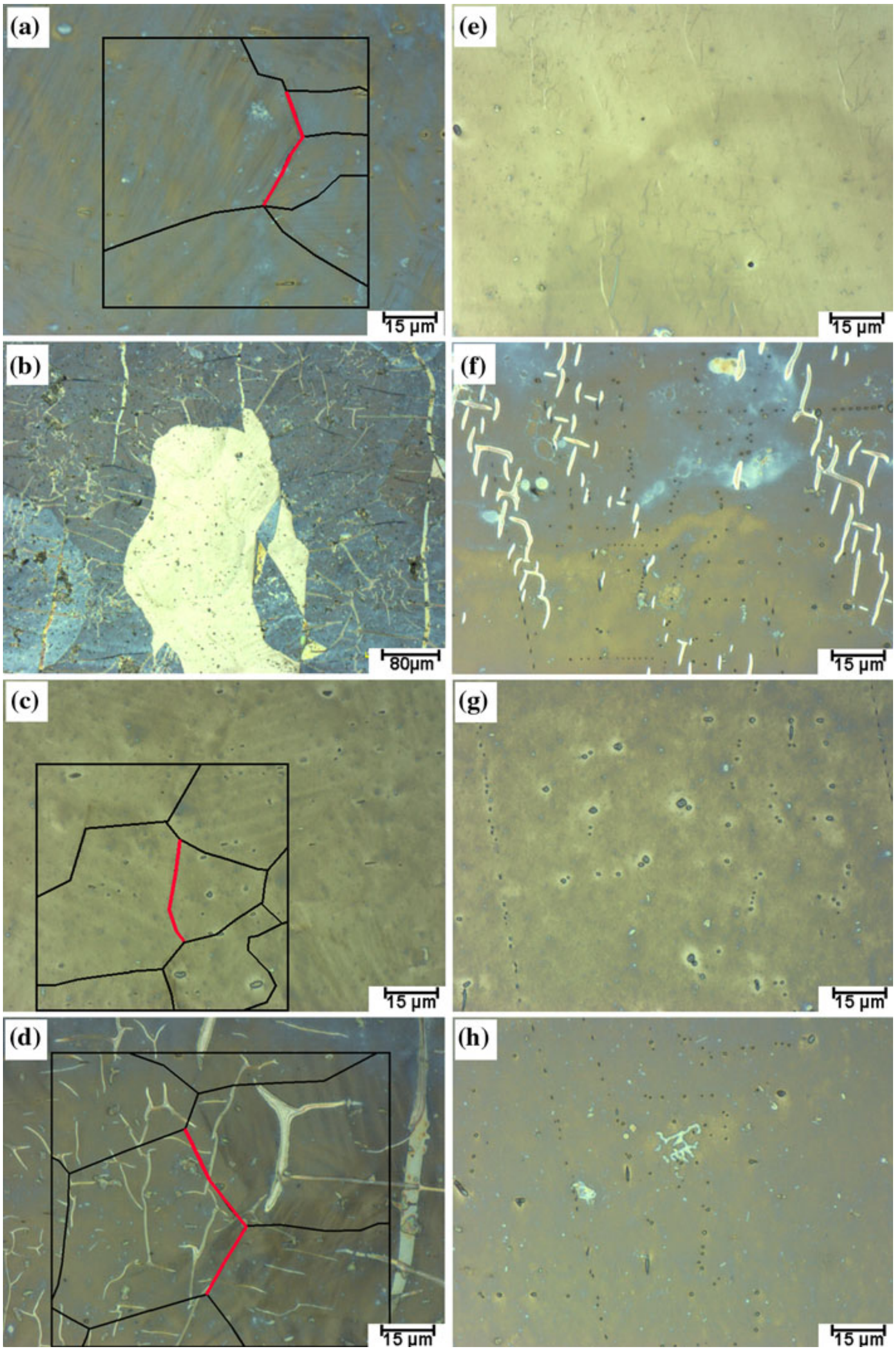

Fig. 5 Light optical images recorded subsequent to mechanical testing from polycrystalline (**a**–**d**) and single crystal substrates (**e**–**h**) coated with **a** + **e** $[PAA/PAH]_{10}$-pH7, **b** + **f** $[PAA/PAH]_{10}$-pH7-cured, **c** + **g** $[MMT/PAA/PAH]_{10}$-pH7, and **d** + **h** $[MMT/PAA/PAH]_{10}$-pH7 + cured polyelectrolyte films. For the polycrystalline substrates, microstructure details are superimposed. Critical grain boundaries determined based on topography data (Fig. 4) are plotted in *red*. Loading direction is *horizontal* for all the shown images (Color figure online)

in good agreement with AFM-measurements reported before [47]. After mechanical testing in Hank's solution, a distinct increase of surface roughness up to a RMS value of 6.7 nm was observed including a distinct elevation in the center of Fig. 6b. This may be attributed to local buckling because of substrate surface topography as well as by swelling and precipitation caused by immersion in Hank's solution. However, the most important finding is that no defects are seen in Fig. 6b. This was confirmed by an extended set of measurements attesting to the excellent formability of the polyelectrolytes reinforced with nano-clay-platelets.

Discussion

As demonstrated by the in situ EBSD and CLSM data in Fig. 3, martensitic variants of different geometric dimensions nucleate in the polycrystalline and the single crystal substrates. Moreover, the martensite morphologies deviate

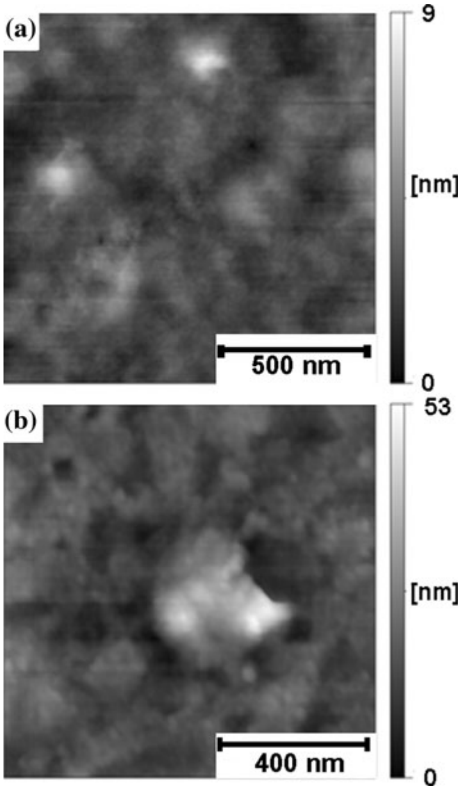

Fig. 6 AFM images of a [MMT/PAA/PAH]$_{10}$-pH7-coated polycrystalline substrate **a** before and **b** after 300 cycles with 5% macroscopic maximum strain per cycle

for forward and reverse transformations. It has been reported before that topographic effects at phase boundaries may be explained based on geometric and interfacial properties of the martensitic domains [48]. Furthermore, the equilibrium martensitic domain geometry is dependent on the elastic strain energy present at the phase boundaries as well as the surface energy of the martensitic domain [48–50]. The aspect ratio of martensitic domains is crucial for the surface energy [48]. The maximum domain length is basically determined by the grain size in polycrystalline samples and by the sample width in case of single crystals. Consequently, martensitic plate lengths in the range of some microns and some millimeters are observed in polycrystalline samples and the single crystals, respectively. As the surface energy can be reduced by an advantageous aspect ratio, wider domains are present in single crystals. From AFM-measurements [51, 52] it can be seen that the domain width determines relief heights because of a tilt of the surface from the austenitic to the martensitic phase. While theoretical and experimental investigations revealed that different martensitic variants result in different tilt angles ranging from 4 to 13° [45, 51–53], wider domains always resulted in elevated topography at phase boundaries ranging from 60 nm to 3 µm [48, 52, 53]. Figure 3 reveals that fewer but wider fronts are active during reverse transformation in NiTi. Both the higher topography in the single crystals as well as the elevated topography during reverse transformations can be explained based on the geometric aspects of the martensite domains.

For the defect formation in the coatings, two more aspects of martensite nucleation and propagation have to be considered. It has been reported that topographic effects in NiTi remain stable during mechanical cycling [48] although domain fronts may become less clear. In addition, Tirry et al. [45] reported that, based on in situ TEM observations, during repeated loading and unloading martensite plates always nucleate at the same position and grow in the same direction. This indicates that topographic effects at phase boundaries are localized and repeated during mechanical cycling. Therefore, phase boundaries in single crystal NiTi are most critical for the formability of the applied films, while grain boundary-induced topographies are determining defect formation in polycrystals where the phase boundary reliefs are less prominent. Thus, for the envisaged applications of coated NiTi substrates, an adjustment of the substrate microstructure with respect to texture and grain size is needed to reduce phase or grain boundary-induced topography effects.

Obviously, nanoclay-reinforced films demonstrated enhanced formability as compared to unmodified [PAA/PAH]$_{10}$-pH7, while cured films exhibited an extensive formation of defects (Fig. 5). Clearly, the different deformation properties of the films have to be related to the mechanical behavior of the substrate, but there is also an impact of the saline solutions to the differently modified polyelectrolyte films.

The mechanical properties of weak polyelectrolytes such as [PAA/PAH] are basically determined by the pH-value of the solution during assembly and the resulting chain morphology. For the pH-value used in the present study, high electrostatic intermolecular forces and flattened and extended chains are obtained [54], featuring a Young's modulus of up to 10^8 Pa in the dry state [55]. When treated with pure water, polyelectrolytes demonstrate pronounced swelling, which ranges from 11 to 40% of the initial thickness [41, 56, 57]. Swelling is caused by the water entering through the polyelectrolyte film, diffusing to the hydrophilic regions in the vicinity of charged polymer groups [57], which brings about a remarkable decrease of Young's modulus by one to two orders of magnitude [39, 54, 57]. The presence of salt ions increases the degree of swelling as polymer pairs associate salt ions [58], and thereby the "intrinsic" electrostatic charge compensation is partially replaced by "extrinsic" compensation by the salt ions [40, 59, 60]. For the [PAA/PAH]$_{10}$-pH7 films investigated in the present study, a distinct softening due to swelling in Hank's solution can be assumed, allowing for good accommodation of external strains as the polymer chains become highly mobile [54]. However, owing to the reduced level of crosslinking, defects can form during repeated straining in areas of elevated topographic effects as shown in Fig. 5a, e.

Heating of electrostatically crosslinked polyelectrolyte films to temperatures above 215 °C involves a substitution of the electrostatic COO^{-}/H_3N linkage by a covalent CO–NH bond [26], as schematically shown in Fig. 2. This conversion results in a highly linked and dense chain structure providing an increase of Young's modulus in the range of one order of magnitude [30, 61, 62]. As reported by Pavoor et al. [54], covalent bonds limit the degree of swelling and, hence, the Young's modulus of cured films is still one order of magnitude higher in the swollen state as compared to electrostatically crosslinked [PAA/PAH]. This could explain the high extent of defect formation in thermally cured polyelectrolyte films (Fig. 5b, f), as the polymer chains are less mobile and do not accommodate elevated externally applied strains. Additional experiments demonstrated that even a low covalent bond fraction established by heat treating at 180 °C for 4 h resulted in a similar defect pattern after pseudoelastic cycling in Hank's solution, pointing out the drastic impact of amide bonding on the formability of polyelectrolyte coatings.

Polyelectrolyte films loaded with MMT-nanoclays demonstrated the highest formability during cyclic straining (Fig. 5c, g). Since exfoliated and dispersed nanoplatelets provide a high degree of interfacial electrostatic interaction with the polymer chains, the modulus of the composites increases remarkably as reported for several polymer–clay systems (e.g., [31, 63–66]). Interestingly, the increase of stiffness is accompanied by an enhanced elongation to failure, which is attributed to a more "dangling" chain formation and conformational effects at the clay–matrix interface [31]. Furthermore, the degree of water uptake can be limited by clay loading [32, 67]. Hence, the improved stiffness, elongation to failure, and the reduced sensitivity to swelling-related softening explains the integrity of the $[MMT/PAA/PAH]_{10}$-pH7 films after mechanical testing in Hanks's solution. The combination of thermal curing and nanoclay reinforcement is known to further increase Young's modulus; however, the elongation to failure is reduced [68, 69], which can be attributed to covalent bondings.

For biomedical applications of the polyelectrolyte films as protective coatings on NiTi substrates other aspects, such as the impact of body temperature on the swelling behavior or the barrier properties, have to be considered. Interestingly, clay loading [32] and thermal curing [36] have already demonstrated to improve the barrier properties as well as enhancing wear resistance [70, 71]. Given the observed excellent formability of the nanoclay-reinforced systems, modified polyelectrolyte films appear to be promising candidate materials for biomedical applications.

Conclusions

The present study establishes a clear relation between phase transformation characteristics in polycrystalline and single crystal NiTi SMAs and the defect formation in thin polyelectrolyte films applied onto these substrates. Moreover, the differences in formability of unmodified, thermally cured, and nanoclay-reinforced polyelectrolyte films can be related to their chemical characteristics and their swelling behavior in saline media. The main results can be summarized as follows:

1) Elevated phase boundary topographies emerge in single crystals as compared with polycrystals, which can be related to interfacial and geometric features of the martensite domains.
2) Phase boundary related topographic evolution governs the defect formation in polyelectrolytes applied on single crystal substrates. In contrast, defects in thin polyelectrolyte films emerge predominantly in the vicinity of critical grain boundaries, in case of polycrystalline samples.
3) Thermal curing treatment decreased the formability of the polyelectrolyte films remarkably because of the formation of less mobile covalently bonded chains.
4) Nanoclay-reinforced, highly electrostatically crosslinked films demonstrated superior formability on both substrates employed.

Acknowledgements The authors thank Philipp Krooß, Hans-Christian Schmidt, and Christian Kunze for their help with the measurements. Prof. Chumlyakov is thanked for providing the single crystals. Financial support by the Deutsche Forschungsgemeinschaft is gratefully acknowledged.

References

1. Chen MF, Yang XJ, Liu Y, Zhu SL, Cui ZD, Man HC (2003) Surf Coat Technol 173:229–234
2. Kujala S, Pajala A, Kallioinen M, Pramila A, Tuukkanen J, Ryhänen J (2004) Biomaterials 25:353–358
3. Duerig TW, Wholey M (2002) Minim Invasive Ther Allied Technol 11:173–178
4. Feninat FE, Laroche G, Fiset M, Mantovani D (2002) Adv Eng Mater 4:91–104
5. Pelton AR, Stöckel D, Duerig TW (2000) Mater Sci Forum 327–328:63–70
6. Sunderman FW (1977) Ann Clin Lab Sci 7:377–398
7. Morgan NB (2004) Mater Sci Eng 378:16–23
8. Assad M, Chernyshov AV, Jarzem P, Leroux MA, Coillard C, Charette S, Rivard CH (2003) J Biomed Mater Res B Appl Biomater 64B:121–129

9. Bishara SE, Barrett RD, Selim MI (1993) Am J Orthod Dentofac Orthop 103:115–119
10. Carroll WM, Kelly MJ (2003) J Biomed Mater Res B 67B:1123–1130
11. Cissé O, Savadogo O, Wu M, Yahia LH (2002) J Biomed Mater Res 61:339–345
12. Venugopalan R, Trépanier C (2000) Minim Invasive Ther Allied Technol 9:67–74
13. Riepe G, Heintz C, Kaiser E, Chakfe N, Morlock M, Delling M, Imig H (2002) Eur J Vasc Endovasc Surg 24:117–122
14. Pohl M, Glogowski T, Kühn S, Hessing C, Unterumsberger F (2008) Mater Sci Eng 481–482:123–126
15. Shabalovskaya SA, Tian H, Anderegg JW, Schryvers DU, Carroll WU, Van Humbeeck J (2009) Biomaterials 30:468–477
16. Cheng Y, Zheng YF (2006) Mater Sci Eng 438–440:1146–1149
17. Sui JH, Cai W (2006) Nucl Instrum Methods Phys Res 251:402–406
18. Xu JL, Liu F, Wang FP, Yu DZ, Zhao LC (2009) Curr Appl Phys 9:663–666
19. Heßing C, Frenzel J, Pohl M, Shabalovskaya S (2008) Mater Sci Eng 486:461–469
20. Frotscher M, Neuking K, Böckmann R, Wolff KD, Eggeler G (2008) Mater Sci Eng 481–482:160–165
21. Lackmann J, Regenspurger R, Maxisch M, Grundmeier G, Maier HJ (2010) J Mech Behav Biomed Mater 3:436–445
22. Decher G, Hong JD, Schmitt J (1992) Thin Solid Films 210–211:831–835
23. Decher G (1997) Science 277:1232–1237
24. Hammond PT (2004) Adv Mater 16:1271–1293
25. Jaber JA, Schlenoff JB (2006) Curr Opin Coll Interface Sci 11:324–329
26. Dai J, Sullivan DM, Bruening ML (2000) Ind Eng Chem Res 39:3528–3535
27. Antipov AA, Sukhorukov GB, Möhwald H (2003) Langmuir 19:2444–2448
28. Shiratori SS, Rubner MF (2000) Macromolecules 33:4213–4219
29. Lackmann J, Niendorf T, Maxisch M, Grundmeier G, Maier HJ (2011) Mater Charact 62:298–303
30. Richert L, Engler AJ, Discher DE, Picart C (2004) Biomacromolecules 5:1908–1916
31. Wang Z, Pinnavaia TJ (1998) Chem Mater 10:3769–3771
32. Heidarian M, Shishesaz MR, Kassiriha SM, Nematollahi M (2010) Prog Org Coat 68:180–188
33. Sehitoglu H, Hamilton R, Canadinc D, Zhang XY, Gall K, Karaman I, Chumlyakov Y, Maier HJ (2003) Metall Mater Trans A 34:5–13
34. Gall K, Maier HJ (2002) Acta Mater 50:4643–4657
35. Liu Y, Yang H (1999) Mater Sci Eng A 260:240–245
36. Harris JJ, DeRose PM, Bruening ML (1999) J Am Chem Soc 121:1978–1979
37. Yamagata Y, Shiratori S (2003) Thin Solid Films 438–439: 238–242
38. Choubey A, Balasubramaniam R, Basu B (2004) J Alloys Compd 381:288–294
39. Nolte AJ, Rubner MF, Cohen RE (2005) Macromolecules 38: 5367–5370
40. Heuvingh J, Zappa M, Fery A (2005) Langmuir 21:3165–3171
41. Tanchak OM, Barrett CJ (2004) Chem Mater 16:2734–2739
42. Günzler H, Gremlich HU (2003) IR-Spektroskopie, 4th edn. Wiley-VCH, Weinheim
43. Titz T, Hörzenberger F, Van den Bergh K, Grundmeier G (2010) Corros Sci 52:369–377
44. Özkaya B, Özcan Ö, Thissen P, Grundmeier G (2010) Langmuir 26(11):8155–8160
45. Tirry W, Schryvers D (2008) Mater Sci Eng A 481–482:420–425
46. Daly S, Ravichandran G, Bhattacharya K (2007) Acta Mater 55:3593–3600
47. Dai X, Zhang Y, Guan Y, Yang S, Xu J (2005) Thin Solid Films 474:159–164
48. Feng P, Sun QP (2006) J Mech Phys Solids 54:1568–1603
49. Maciejewski G, Stupkiewicz S, Petryk H (2005) . Arch Mech 57(4):277–297
50. Messner C, Reisner G, Sun QP, Werner E (2000) Comput Mater Sci 19:313–319
51. Liu DZ, Kikuchi T, Kajiwara S, Shinya N (1999) J Intell Mater Syst Struct 10:569–574
52. Liu DZ, Kajiwara S, Kikuchi T, Shinya N (2002) Mater Sci Forums 394–395:193–200
53. Yang Z, Fang H, Wang J, Li C, Zheng Y (1995) Phys Rev B 52:7879–7882
54. Pavoor PV, Bellare A, Strom A, Yang D, Cohen RE (2004) Macromolecules 37:4865–4871
55. Thompson MT, Berg MC, Tobias IS, Rubner MF, Van Vliet KJ (2005) Biomaterials 26:6836–6845
56. Decher G, Lvov Y, Schmitt J (1994) Thin Solid Films 244: 772–774
57. Nolte AJ, Treat ND, Cohen RE, Rubner MF (2008) Macromolecules 41:5793–5798
58. Dubas ST, Schlenoff JB (2001) Langmuir 17:7725–7727
59. Farhat TR, Schlenoff JB (2001) Langmuir 17:1184–1192
60. Jaber J, Schlenoff JB (2006) J Am Chem Soc 128:2940–2947
61. Francius G, Hemmerle J, Ohayon J, Schaaf P, Voegel J, Picart C, Senger P (2006) Microsc Res Tech 69:84–92
62. Schneider A, Vodouhe C, Richert L, Francius G, Le Guen E, Schaaf P, Voegel J, Frisch B, Picart C (2007) Biomacromolecules 8:139–145
63. Dong Y, Bhattacharyya D (2008) Compos A 39:1177–1191
64. Chang JH, An YU, Cho D, Giannelis EP (2003) Polymer 44:3715–3720
65. Ma J, Zhang S, Qui Z (2001) J Appl Polym Sci 82:1444–1448
66. Ramorino G, Bignotti F, Pandini S, Ricco T (2009) Compos Sci Technol 69:1206–1211
67. Giannelis EP (1996) Adv Mater 8:29–35
68. Delozier DM, Orwoll RA, Cahoon JF, Johnston NJ, Smith JG Jr, Connell JW (2002) Polymer 43:813–822
69. Zulfiqar S, Sarwar MI (2008) Scripta Mater 59:436–439
70. Bakshi SR, Balani K, Laha T, Tercero J, Agarwal A (2007) J Manage 59:50–53
71. Yusoh K, Jin J, Song M (2010) Prog Org Coat 67:220–224